



Carbon nanofibers decorated with FeO_x nanoparticles as a flexible electrode material for symmetric supercapacitors

Edmund Samuel ^{a,1}, Bhavana Joshi ^{a,1}, Hong Seok Jo ^a, Yong Il Kim ^a, Seongpil An ^a, Mark T. Swihart ^b, Je Moon Yun ^c, Kwang Ho Kim ^{c,d,*}, Sam S. Yoon ^{a,*}

^a School of Mechanical Engineering, Korea University, Seoul 02841, Republic of Korea

^b Department of Chemical & Biological Engineering, University at Buffalo, The State University of New York, Buffalo, New York 14260-4200, USA

^c Global Frontier R&D Center for Hybrid Interface Materials, Pusan National University, San 30 Jangjeon-dong, Geumjeong-gu, Busan 609-735, Republic of Korea

^d School of Materials Science and Engineering, Pusan National University, San 30 Jangjeon-dong, Geumjeong-gu, Busan 609-735, Republic of Korea

HIGHLIGHTS

- Highly flexible FeO_x -carbon nanocomposite nanofibers were fabricated.
- Freestanding FeO_x -CNF showed excellent retention (89%) after 5000 cycles at $1 \text{ A}\cdot\text{g}^{-1}$.
- A FeO_x /CNF-based supercapacitor provides $436 \text{ F}\cdot\text{g}^{-1}$ of capacitance at $1 \text{ A}\cdot\text{g}^{-1}$.
- Excellent uniform decoration of CNF with FeO_x was demonstrated.

ARTICLE INFO

Article history:

Received 16 March 2017

Received in revised form 10 July 2017

Accepted 11 July 2017

Available online 12 July 2017

Keywords:

Electrospinning

FeO_x

Carbon nanofiber

Binder free

Supercapacitor

ABSTRACT

We have produced flexible, freestanding, and light weight mats of FeO_x -decorated carbon nanofibers (CNFs) and demonstrated their use in supercapacitors with high energy and power density and excellent long term capacitance retention. Highly flexible carbon-iron oxide nanofibers were synthesized by electrospinning a solution of polyacrylonitrile (PAN), polymethylmethacrylate (PMMA), and iron acetylacetate (FeAcAc), followed by annealing to carbonize the PAN, pyrolyze the PMMA to produce pores, and convert FeAcAc to FeO nanoparticles. The morphology of the FeO_x /CNF composite was determined by scanning and transmission electron microscopies, which showed that the embedded FeO_x nanoparticles were well distributed in the CNF electrode. We employed cyclic voltammetry, galvanostatic charge/discharge measurements, and electrochemical impedance spectroscopy to evaluate the electrochemical performance of symmetric supercapacitors prepared from the FeO_x /CNF composite. The supercapacitors exhibited high specific capacitance ($427 \text{ F}\cdot\text{g}^{-1}$ at $10 \text{ mV}\cdot\text{s}^{-1}$ and $436 \text{ F}\cdot\text{g}^{-1}$ at $1 \text{ A}\cdot\text{g}^{-1}$ in the optimal case) and good stability, retaining 89% of their initial capacitance after 5000 cycles at a current density of $1 \text{ A}\cdot\text{g}^{-1}$. The optimal device achieved an energy density of $167 \text{ Wh}\cdot\text{kg}^{-1}$ at a power density of $0.75 \text{ kW}\cdot\text{kg}^{-1}$, and an energy density of $66 \text{ Wh}\cdot\text{kg}^{-1}$ at a power density of $7.5 \text{ kW}\cdot\text{kg}^{-1}$. These combinations of energy and power densities can meet the needs of many emerging supercapacitor applications.

© 2017 Elsevier B.V. All rights reserved.

1. Introduction

Supercapacitors (SCs) can provide high power density and long cycle life for energy storage, features that are useful in hybrid elec-

* Corresponding authors at: Global Frontier R&D Center for Hybrid Interface Materials, Pusan National University, San 30 Jangjeon-dong, Geumjeong-gu, Busan 609-735, Republic of Korea (K.H. Kim).

E-mail addresses: kwhokim@pusan.ac.kr (K.H. Kim), skyoon@korea.ac.kr (S.S. Yoon).

¹ These authors have contributed equally.

tric vehicles and many portable devices. The charge-storage mechanisms of SCs include electric double layer capacitance (EDLC) and pseudocapacitance. The EDLC is exhibited by high surface area carbon-based materials, wherein charge is stored electrostatically at the electrode/electrolyte interface, and the transfer of electrons is not involved. On the other hand, pseudocapacitance is mainly observed in conducting polymers (such as polyaniline and polypyrrole) and transition metal oxides, which exhibit fast surface Faradaic reactions. Capacitors that rely entirely on EDLC have relatively low energy density, i.e., low specific capacitance. Pseudo-

capacitance materials provide higher energy density, but have lower power density, because their discharge rates are limited by the rates of Faradaic reactions, rather than simply the motion of ions. Properly combining these two types of materials [1] can significantly improve supercapacitor performance in terms of combined specific capacitance (energy density) and rate capability (power density).

Among the various metal oxides that can be used as electrode materials in SCs, iron oxide may be the most promising, as it is environmentally friendly, has a high capacitance, is low cost, and exhibits a pseudocapacitance nature. However, the primary drawback of iron oxide is its poor rate capability and intrinsically low conductivity (10^{-14} S·cm $^{-1}$). Graphitic carbon, in the form of graphene, carbon nanotubes (CNTs), or carbon nanofibers (CNF) can be used to increase the conductivity and charge transfer rate of pseudocapacitive materials.[2] Addition of high surface area carbon also ensures that the materials exhibit both EDLC and pseudocapacitance.

Carbon/iron oxide composite electrodes for SCs have been previously investigated in several studies. Ullah et al. [3] prepared an iron oxide/reduced graphene oxide (rGO) composite by a hydrothermal method. The composite exhibited a specific capacitance of 287 F·g $^{-1}$ at a scan rate of 5 mV·s $^{-1}$ in 1 M KOH. Fu et al. [4] hydrothermally synthesized Fe₃O₄ over CNFs with a necklace-like architecture. The Fe₃O₄/CNF composite was spray-coated on stainless steel along with a conductive additive (carbon black). These electrodes showed a specific capacitance of 225 F·g $^{-1}$ at a current density of 1 A·g $^{-1}$. Liu et al. [5] fabricated a nitrogen-doped rGO/iron oxide composite by the hydrothermal process and formed a working electrode by coating a slurry of the composite onto Ni foam. The electrode showed a specific capacitance of 268.4 F·g $^{-1}$ at a current density of 2 A·g $^{-1}$ in 1 M KOH. Binitha et al. [6] prepared electrospun Fe₂O₃ nanostructures using a precursor of polyvinyl acetate, polyvinyl pyrrolidone, and ferric acetyl acetonate. The fabricated NFs were annealed in air and then electrophoretically deposited on Ni foil. The resulting material showed a specific capacitance of 256 F·g $^{-1}$ at a scan rate of 5 mV·s $^{-1}$ in 1 M LiOH. Most studies of composite electrodes have employed a binder and conductive additives during deposition onto a current collector. However, when these flexible electrodes are employed in

practical applications, the active material may detach from the current collector, degrading their performance. In addition, the use of a current collector increases the total weight of the electrode. Furthermore, most binders are electrically insulating and inevitably reduce the conductivity of the composite, degrading its performance [7]. A few studies have been reported on the fabrication of binder-free and flexible Fe₂O₃ electrodes for use in SCs [7–9]. However, the performance observed in those studies did not meet commercial requirements.

In the present study, we applied the electrospinning technique to create FeO_x/CNF composites. A blend of PAN and PMMA with iron(III) acetylacetone was used for the electrospinning process. After annealing of the electrospun fiber mats, FeO_x nanoparticles were uniformly anchored on the carbon nanofiber matrix, while PMMA was pyrolyzed to create meso-scale pores within the carbon nanofibers [10]. The resulting nanocomposite electrodes required no current collector or other substrate, and contained no binders or additives. Furthermore, the fabricated supercapacitor electrodes are flexible and freestanding, which expands their potential for use in portable flexible electronic applications. The enhanced electrolyte diffusion and ion transport of the FeO_x-decorated CNFs is demonstrated and explained in the following sections. The corresponding performance of the electrodes in specific capacitance, energy and power density are presented.

2. Experimental procedures

In a typical process, PAN (Mw = 150 kDa; Sigma-Aldrich) and PMMA (Mw ~ 120 kDa; Sigma-Aldrich) were dissolved in N, N-dimethylformamide (DMF; 99.8%; Sigma-Aldrich), and the mixture was stirred for 24 h at 60 °C. The PMMA concentration was varied at 0, 0.5, 1.5, and 2.5 wt% with respect to PAN. The total weight percent of the entire polymer (PAN + PMMA) in the solution was 10 wt% for all samples. Then, 4 wt% iron(III) acetylacetone (Fe(C₅H₇O₂)₃, Sigma-Aldrich) was dissolved in this PAN/PMMA–DMF solution, and the resulting mixture was stirred again for 24 h at room temperature to form a homogeneous solution. The samples with PMMA contents of 0, 0.5, 1.5, and 2.5 wt% are labeled as F0, F1, F2, and F3, respectively. The solution was loaded into a syringe with a needle (ID = 0.84 mm, OD = 1.27 mm)

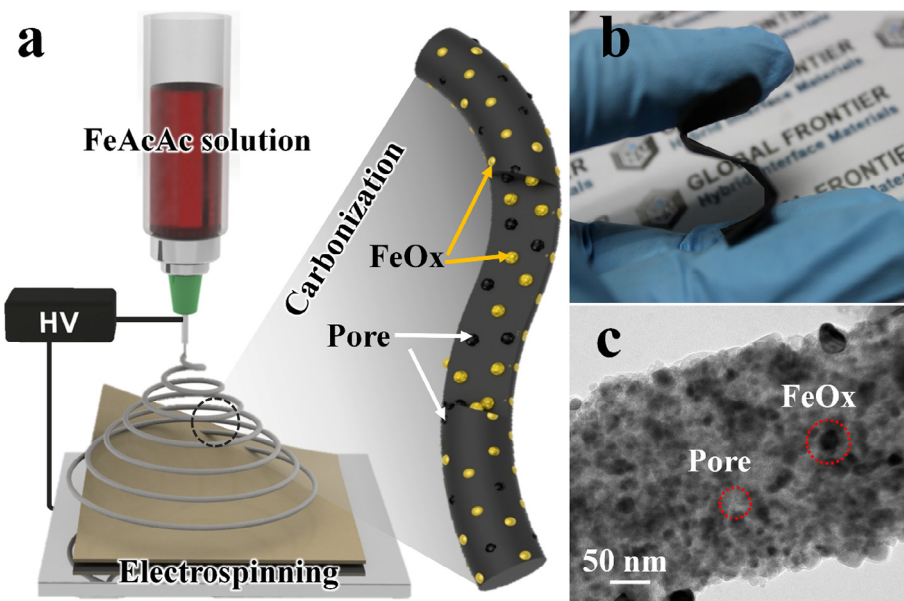


Fig. 1. (a) Schematics of electrospinning setup used and a CNF, (b) highly flexible FeO_x/CNF composite mat, and (c) TEM image of FeO nanoparticles embedded on a CNF and the pores present in the CNF.

for electrospinning. Then, using a syringe pump, fibers of the solution were deposited on a grounded collector while applying a high voltage (7 kV) to the needle to ensure a stable Taylor cone at the end of the needle. The needle-to-substrate distance was 13 cm. The electrospinning setup is shown in Fig. 1a. The electrospun mats were stabilized in air at 280 °C for 1 h and then subjected to annealing in a tube furnace in a flow of Ar at 800 °C for 1 h. The obtained carbonized samples were freestanding and flexible, as shown in Fig. 1. Fig. 1c shows a transmission electron microscopy (TEM) image of a carbon nanofiber decorated with FeO_x nanoparticles.

Electrochemical measurements were performed using a two-electrode symmetric coin cell (CR2032), in which the carbonized

electrospun composite mats were used for both electrodes. The electrodes were punched into a circular shape with an area of 1.54 cm². A polymer film (3501 Celgard, Chungbuk, South Korea) was used as a separator between the electrodes and 1 M Na₂SO₄ as the electrolyte. A potential window of –1.2 to 0.3 V was used for the cyclic voltammetry (CV) measurements, which were performed at different scan rates (2, 5, 10, 20, 30, 50, and 100 mV·s^{–1}). The galvanostatic charge/discharge tests were carried out at current densities of 0.5, 1, 2, 3, and 5 A·g^{–1}. Two symmetric supercapacitors with a dimension of 2 cm × 3 cm in series were used to light an LED (light emitting diode).

3. Results and discussion

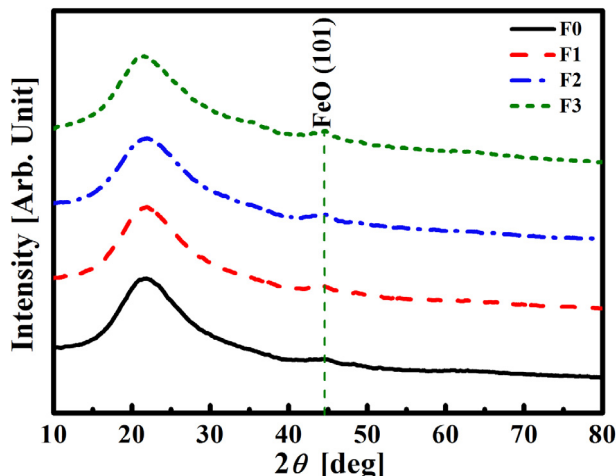


Fig. 2. X-ray diffraction patterns of various FeO/CNF composites.

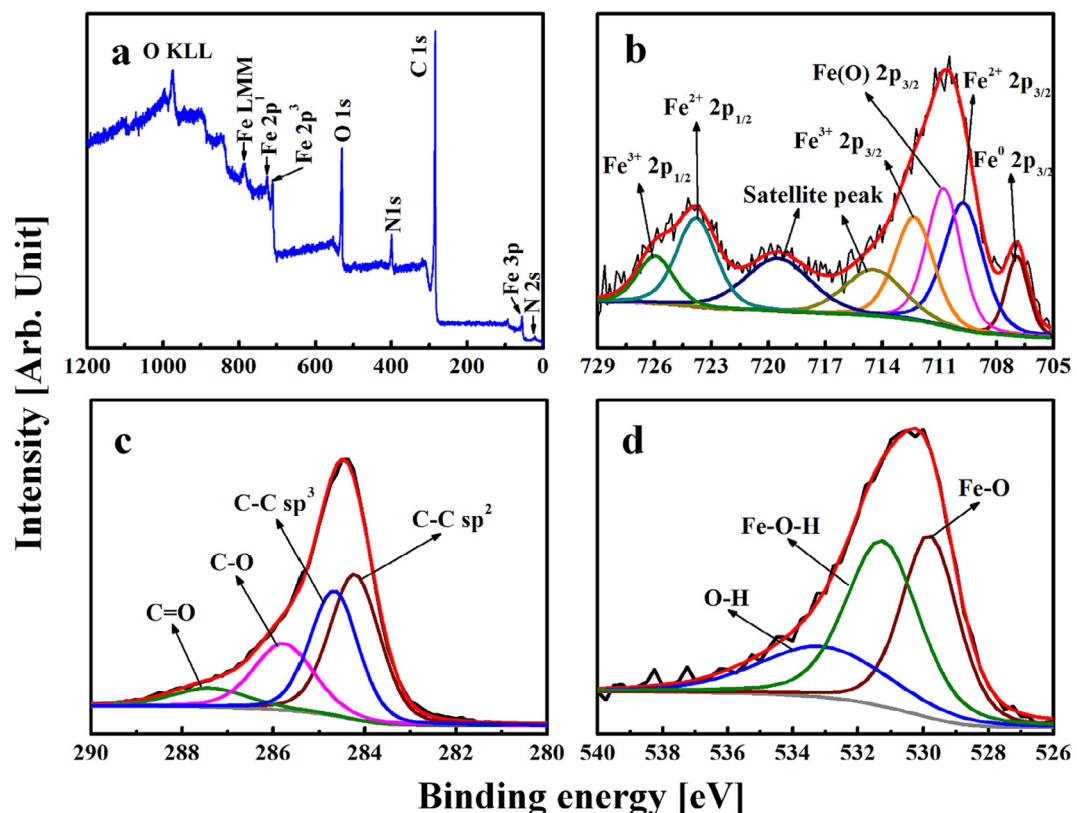


Fig. 3. (a) XPS survey spectrum of composite F2 and the corresponding deconvoluted high-resolution XPS spectra for (b) Fe2p, (c) C1s, and (d) O1s.

the complete survey spectrum for sample F2, which shows carbon, oxygen, nitrogen, and iron. The atomic concentration of the elements determined from the XPS survey spectrum was C 1s ~ 72%, O 1s ~ 17.9%, N 1s ~ 7.6%, and Fe 2p ~ 2.5%. The Fe 2p XPS spectrum, shown in Fig. 3b, contains two peaks, which are located at 710.5 and 724.2 eV and correspond to Fe^{2+} 2p_{3/2} and Fe^{2+} 2p_{1/2}, respectively. The difference in the energies of the Fe^{2+} 2p_{3/2} and Fe^{2+} 2p_{1/2} peaks is 13.7 eV. The peak at 710.5 eV could be deconvoluted into three peaks, which were located at 709.7, 710.7, and 712.5 eV. In addition, a shoulder peak at a lower binding energy (707.1 eV) can also be seen in Fig. 3b, which is indicative of metallic Fe. The binding energy for FeO ranges from 709.7 to 710.7 eV, that for Fe_3O_4 ranges from 707.1 to 710.7 eV, and that for Fe_2O_3 ranges from 710.7 to 712.5 eV. The charge-transfer-related satellite peaks are indicative of the actual oxidation state of iron. For Fe^{2+} (FeO), the satellite peak appears at a lower binding energy (714.6 eV), whereas for Fe^{3+} the satellite peak appears at (719.5 eV) with peak satellite separation of 5.4 and 8.8 eV respectively. [15] The percentage of FeO, Fe_3O_4 and Fe_2O_3 in FeO_x is 44, 16, and 40% respectively, as determined from peak area ratios of the deconvoluted Fe 2p XPS spectra. In the C1s spectrum (see Fig. 3c), the peaks at 284.25, 284.75, 285.8, and 287.5 eV correspond to C=C sp², C=C sp³, C=O, and C=O bonds respectively. In the O1s spectrum (see Fig. 3d), the peak at 530 eV is attributable to the formation of Fe–O, while the two shoulder peaks located at 531.25 and 533.25 eV are related to Fe–O–H and surface –OH moieties, respectively. The deconvoluted N1s spectrum, presented in Fig. S1, shows the presence of graphitic nitrogen. The presence of tertiary nitrogen bonding deduced from the data in Fig. S1 implies that one of the graphitic carbon atoms was replaced with nitrogen.

The structures of the FeO_x /CNF composite samples were examined by field-emission scanning electron microscopy (FE-SEM) (S-5000, Hitachi, Ltd.), as shown in Fig. 4. The fibers were round and fully interconnected and exhibited a uniform diameter distribution. Further, in all cases, the FeO_x nanoparticles are well distributed over the surfaces of the CNFs. The electrospun CNF

composites also contain voids; this promotes rapid transport of ions within the nanofiber mat. In addition, the FeO_x nanoparticles did not undergo aggregation, and remained as discrete particles with diameters below 50 nm. A small particle size allows for better contact with the electrolyte. Low magnification SEM images of all samples are presented in Fig. S2. Finally, the average diameters of the fibers in samples F0, F1, F2 and F3 are 360, 340, 320 and 290 nm, respectively, as determined from the SEM images shown in Fig. S3. The atomic percent of elements of the F2 composite (Fig. S3e) determined by energy-dispersive X-ray spectroscopy configured with SEM are C ~ 54%, O ~ 21%, N ~ 16%, and Fe ~ 8%.

The Raman spectra of the FeO_x /CNF composites are shown in Fig. 5. The characteristic peaks of FeO could not be seen clearly between wavenumbers of 200–800 cm⁻¹ (see Fig. S4), indicating the presence of an amorphous or ultrafine nanocrystalline phase. However, the broad D and G bands, seen at 1356 and 1590 cm⁻¹, respectively, are attributable to the graphene phase of the CNFs.

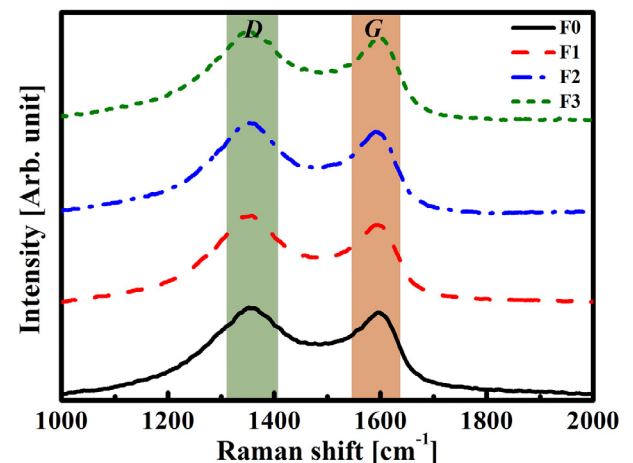


Fig. 5. Raman spectra of freestanding FeO_x /CNF composites.

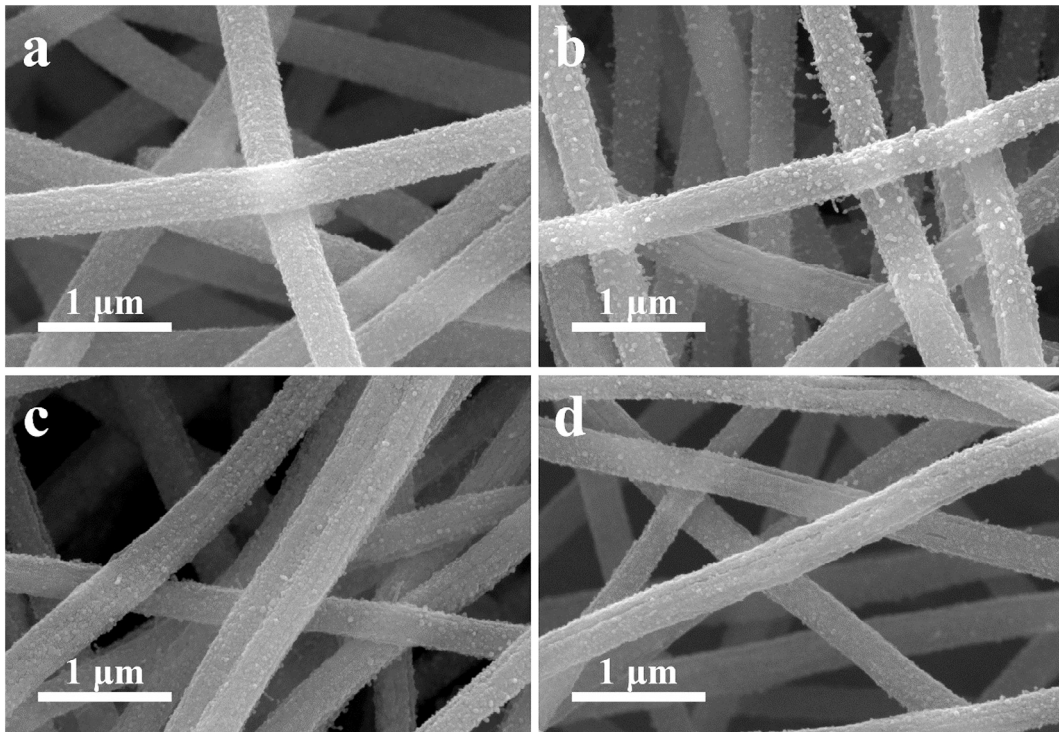


Fig. 4. SEM images of samples (a) F0, (b) F1, (c) F2 and (d) F3.

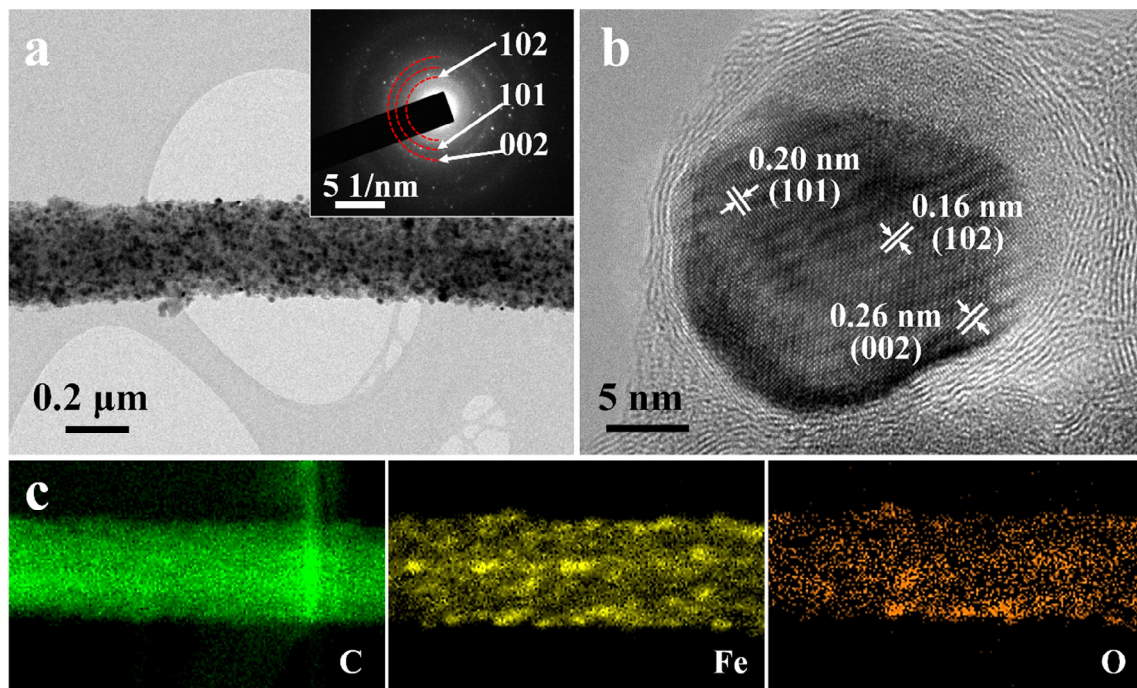


Fig. 6. (a) TEM image of sample F2 (inset shows corresponding SAED pattern), (b) HRTEM image showing interplanar distances for FeO_x , and (c) maps of elements C, Fe, and O for sample F2.

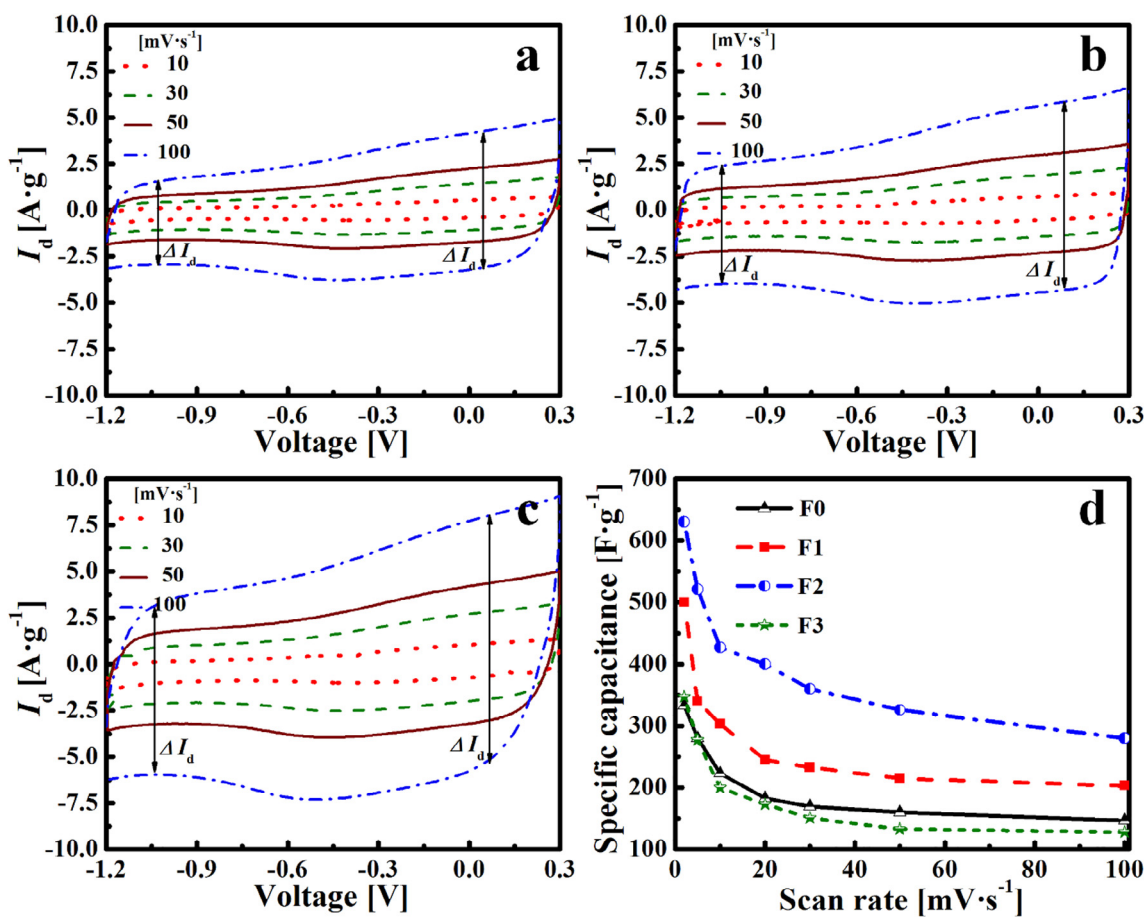


Fig. 7. Current density curves of various FeO_x/CNF composite electrodes measured at different scan rates for potential window of -1.2 to 0.3 V: (a) F0, (b) F1, and (c) F2 and (d) their specific capacitances for different scan rates.

The I_D/I_G ratios for samples F0, F1, F2 and F3 were 1.1, 1.11, 1.04 and 1.07, respectively; these values indicate the presence of defects in the composite samples. The crystalline width, La (nm), can be estimated as $4.4/R$, where $R = I_D/I_G$ [16]. For samples F0, F1, F2 and F3, the width was 4.00, 3.96, 4.23 and 4.11 nm, respectively, suggesting the enhanced crystallinity of F2.

A TEM image (Fig. 6a) of sample F2 shows clearly that the FeO_x nanoparticles are well distributed over the CNFs. The selected area electron diffraction (SAED) pattern is a dot and ring pattern that confirms the polycrystalline nature of the FeO_x/CNF composite. The rings are attributable to the (0 0 2), (1 0 1), and (1 0 2) planes of FeO as per JCPDS card No. 49-1447. Further, the lattice spacing

of 0.26, 0.2, and 0.16 nm as determined from the HRTEM image (Fig. 6b) can be indexed to the (0 0 2), (1 0 1), and (1 0 2) planes of FeO. This further confirms that the FeO nanoparticles were uniformly deposited on the CNFs. Elemental maps obtained using energy-dispersive X-ray spectroscopy (EDX) (Fig. 6c) confirmed the presence of C, Fe, and O, with elements Fe and O being distributed throughout the CNFs. Fig. S5a shows the presence of the pores formed by the PMMA removal during the high-temperature annealing process. These pores are clearly visible as contrasted against a sample without the PMMA addition in Fig. S5b. Furthermore, the formation of pores is also confirmed by the measured N_2 adsorption isotherm as shown in Fig. S6. The

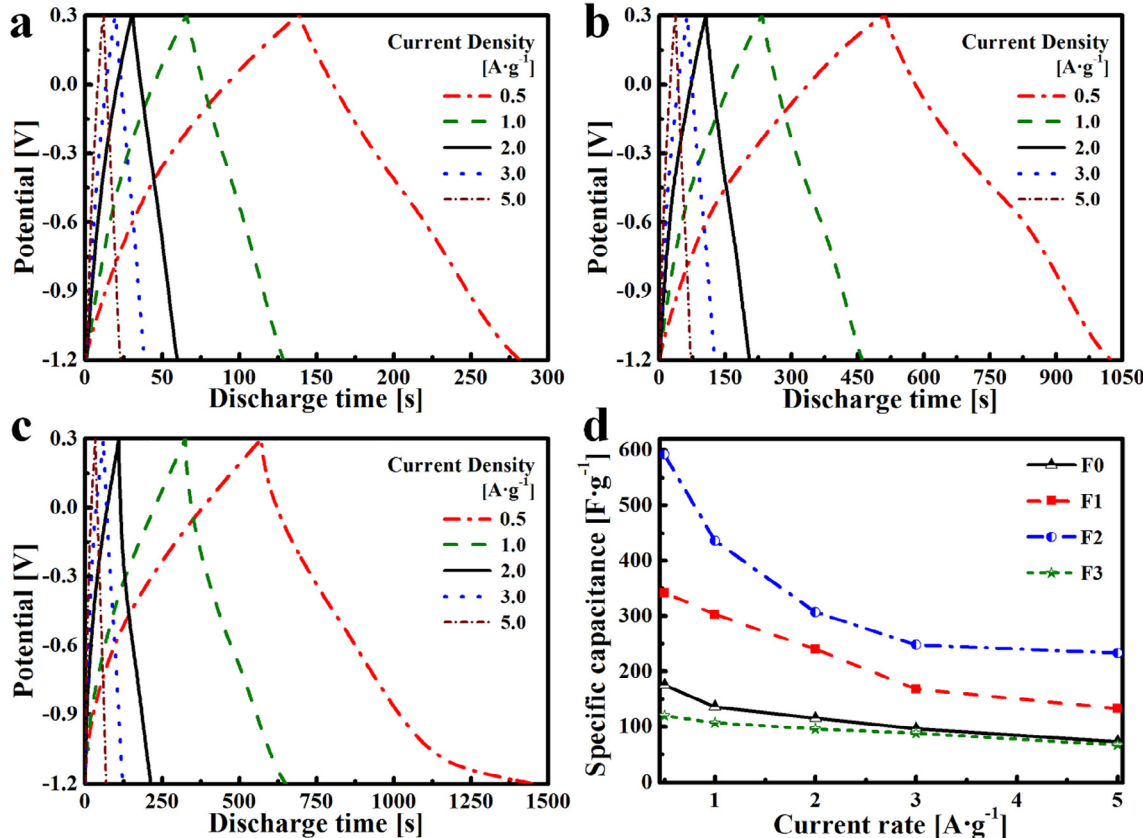


Fig. 8. Galvanostatic charge/discharge curves of various FeO_x/CNF composite electrodes: (a) F0, (b) F1, (c) F2 and (d) their specific capacitances for different current densities.

Table 1
Comparison of specific capacities reported so far with present study.

Materials	Capacitance [$\text{F}\cdot\text{g}^{-1}$]	Scan rate [$\text{mV}\cdot\text{s}^{-1}$]	Current density [$\text{A}\cdot\text{g}^{-1}$]	Potential window [V]	Electrolyte	Refs.
Fe_2O_3	249	–	0.5	−1.4 to 0	1 M KOH	[24]
$\text{Fe}_2\text{O}_3/\text{CNT}$	54	2	–	0 to 0.8	2 M KCl	[25]
$\text{Fe}_3\text{O}_4/\text{C}$	136	–	1	−1.2 to 0	1 M Na_2SO_4	[26]
$\text{Fe}_2\text{O}_3/\text{rGO}$	238	5	–	−1 to 0	1 M Na_2SO_4	[27]
$\text{Fe}_2\text{O}_3/\text{rGO}$	264	–	2.5	−1 to 0	2M KOH	[28]
$\text{Fe}_3\text{O}_4/\text{rGO}$	287	5	–	−0.4 to 1	1 M KOH	[3]
$\text{Fe}_3\text{O}_4/\text{CNF}$	225	–	1	−1.1 to −0.3	3 M KOH	[4]
$\text{Fe}_2\text{O}_3/\text{rGO}$	220	5	–	−1 to 0	1 M Na_2SO_4	[9]
$\text{Fe}_2\text{O}_3/\text{rGO}$	268	–	2	−1 to 0	1 M KOH	[5]
Fe_3O_4	208	–	0.4	−0.9 to 0.1	1 M Na_2SO_3	[29]
$\text{Fe}_2\text{O}_3/\text{CB}$	22	10	–	−0.3 to 0.4	2 M KCl	[30]
$\text{Fe}_2\text{O}_3/\text{Graphene}$	193	5	–	−1.2 to 0.2	1 M Na_2SO_4	[31]
Fe_2O_3	48	5	–	−1 to 0.2	1 M Na_2SO_4	[32]
$\text{Fe}_2\text{O}_3/\text{CB}$	40	10	–	−0.4 to 0.3	2 M KCl	[33]
Fe_2O_3	178	5	–	−0.6 to 0.1	1 M NaOH	[14]
Fe_2O_3	146	5	–	−0.8 to 0	1 M Li_2SO_4	[34]
FeO_x/CNF (F2)	427	10	–	−1.2 to 0.3	1 M Na_2SO_4	Present
FeO_x/CNF (F2)	436	–	1	−1.2 to 0.3	1 M Na_2SO_4	Present

surface area of the composite fibers was determined by the Brunauer–Emmett–Teller (BET) and pore size was estimated by the Barrett–Joyner–Halenda (BJH) method (Table S1).

The applicability of the finely structured FeO_x/CNF nanocomposites as electrode materials in SCs was investigated comprehensively through CV measurements. The potential window of –1.2 to 0.3 V for the symmetric SC was employed to evaluate cyclic voltammetry. The measurements were performed for different scan rates of 2, 5, 10, 20, 30, 50, and 100 $\text{mV}\cdot\text{s}^{-1}$. However, for clarity and ease of analysis, only the CV curves for scan rates of 10, 30, 50, and 100 $\text{mV}\cdot\text{s}^{-1}$ are shown (see Fig. 7a–c). For all scan rates, the curves of current density vs. voltage are almost rectangular. All of the symmetric capacitors based on FeO_x/CNF nanocomposite electrodes exhibited a total potential of 1.5 V. Based on the CV curves, we conclude that the FeO_x/CNF electrode exhibited good pseudocapacitance characteristics. The shape of the CV curve remains unchanged with increasing scan rate, indicating that the electrode also showed good electrochemical reversibility.

Fig. 7a–c shows that the current density increases with the scan rate. However, as shown in Fig. 7d, and as expected for pseudocapacitive electrodes, specific capacitance decreases with scan rate. Electrodes made from sample F2 had the highest specific capacitance, which was $630 \text{ F}\cdot\text{g}^{-1}$ at $2 \text{ mV}\cdot\text{s}^{-1}$; for the same scan rate, the specific capacitances of F0, F1 and F3 were 333, 500 and $331 \text{ F}\cdot\text{g}^{-1}$, respectively. The specific capacitance of F2 remained high at higher scan rates of 10, 30, 50, and $100 \text{ mV}\cdot\text{s}^{-1}$, where specific capacitance was 427, 360, 326, and $280 \text{ F}\cdot\text{g}^{-1}$, respectively. On the other hand, for the same scan rates, the specific capacitances of F0 were 223, 170, 160 and $147 \text{ F}\cdot\text{g}^{-1}$, respectively. Thus, we infer that for a given scan rate, F2 yields a higher current density that also enhances the specific capacitance in comparison with the capacitance of F0 and F1, as depicted in Fig. 7d [17–19]. Note that no signs of any irreversible or non-capacitive Faradaic redox

reactions were observed, which is reasoned with the low crystallinity of FeO_x . Further, highly uniformly distributed FeO_x on carbon nanofibers enhances the surface reaction, which prevented the irreversible redox reaction. In order to demonstrate and quantify the contribution of the pores generated by decomposition of PMMA to the performance of each electrode, the nitrogen adsorption–desorption isotherms of all samples were measured, and results are presented in Fig. S6. The CV curves for all the samples indicated stable electrolyte/electrode performance as a result of rapid ion transport through the electrodes for all scan rates of 10, 30, 50, and $100 \text{ mV}\cdot\text{s}^{-1}$. In the CV curves, their height (or ΔI_d) is relatively smaller toward the negative voltage range, as compared to the height in the positive voltage range. The pores designed by adding PMMA reduces the ion-diffusion pathway, leading to a lower current density (ΔI_d) value as indicated in the CV curves in the negative voltage range. Fig. 7d compares the specific capacitance of the F0, F1, F2, and F3 samples; adding excessive amount of PMMA inflicts the poorest specific capacitance in the F3 sample. Fig. S7a shows the CV curves for F3 for different scan rates while Fig. S7b shows a comparison of the CV curves of F0, F1, F2, and F3 at $10 \text{ mV}\cdot\text{s}^{-1}$.

The galvanostatic discharge curves of the composite electrodes for various current densities are shown in Fig. 8a–c. The curves are linear, indicating that the FeO_x/CNF composites underwent highly reversible Faradaic reactions and exhibited capacitive characteristics. The high capacitance is attributed to a combination of charge storage at the electrolyte/electrode interface and capacitive Faradaic reactions.

In Fig. 8d, the FeO_x/CNF composites exhibited high specific capacitances at fixed current density as well. The specific capacitance of a symmetric supercapacitor can be calculated from these experiments based on the discharge time using the following equation:

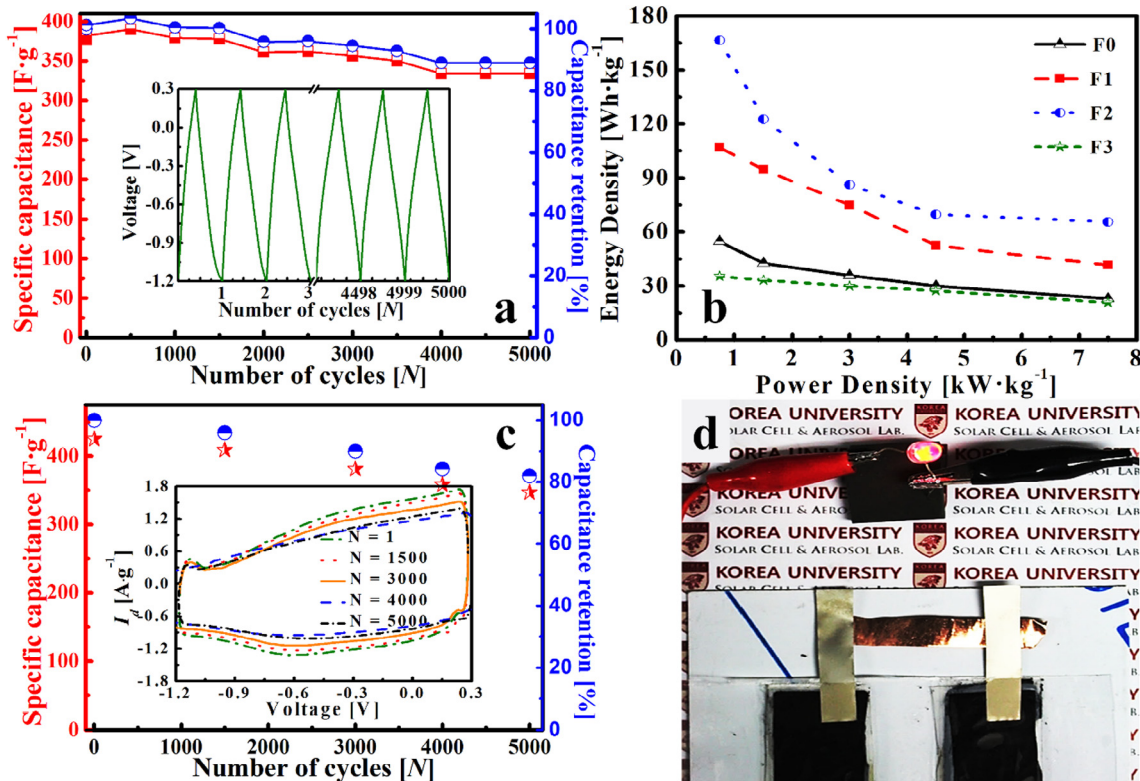


Fig. 9. (a) Cycling performance of F2 at current rate of $1 \text{ A}\cdot\text{g}^{-1}$, (b) Ragone plot depicting power and energy densities of various composite samples, (c) long-term performance of F2-based supercapacitor at scan rate of $10 \text{ mV}\cdot\text{s}^{-1}$, and (d) LED test performed using two flexible symmetric supercapacitors using F2 samples as an electrode. Change Fig. 9b.

$$C_s = \frac{4It}{m(\Delta V - IR)} \quad (1)$$

In Eq. (1) I is the applied current (A), m is the mass of both electrodes (g), t is the discharge time (s), ΔV is the potential window (V), and IR is the voltage drop (V) during the discharging of the supercapacitor. As can be seen from Fig. 8a–c, within the potential window of –1.2 to 0.3 V, no voltage drop (IR) was observed while using 1 M Na₂SO₄ as the electrolyte. However, with a lowering of the PAN content, the Faradaic redox capacitance becomes more prominent than the EDLC, resulting in an increase in the discharge time, as can be seen from Fig. 8b and c. In the case of F2, for a lower current density (0.5 A·g^{−1}), the potential is elongated between –1.15 and –1.2 V; this can be attributed to formation of metallic Fe [20]. Moreover, at lower current density, ion-diffusion covers the maximum possible surface area and hence results in trapping of ions, which caused non-equilibrium condition at the electrode and electrolyte interface. However, diffusion of these ions increased the capacitance after long term cycling [21]. The specific capacitances of F0, F1, F2 and F3 at a current density of 0.5 A·g^{−1} were 175, 342, 592 and 120 F·g^{−1}, respectively while for a current density of 1 A·g^{−1}, they were 136, 303, 436 and 107 F·g^{−1}, respectively (see Fig. 8d). Thus, we conclude that the optimal concentrations of PAN and PMMA for ensuring a high capacitance were 8.5 and 1.5 wt%, respectively. The superior performance of sample F2 could be attributed to the highest surface area (316 m²·g^{−1}), as obtained from BET analysis. The surface areas of all the samples

are given in Table S1. The scan rate, current density, and specific capacitance of the electrodes reported here are significantly higher than those in prior reports, as tabulated in Table 1.

Widening the voltage window of operation of the supercapacitor is desirable, because it increases the energy density. However, widening the voltage window can lead to water decomposition. We adopted two strategies to widen the voltage window without driving water decomposition. First, we used a neutral electrolyte, Na₂SO₄, and Fe, a combination that requires a high over-potential for hydrogen generation. Second, carbon/iron oxide composite electrodes also widen the voltage window without causing electrolyte decomposition. As a result, no significant fading of specific capacitance after 5000 cycles has been observed, which suggests that only minor electrode/electrolyte decomposition may have occurred [22,23].

Fig. 9a shows the specific capacitance of the electrode based on sample F2 and its capacity retention over 5000 cycles, highlighting the long-term performance of the composite. The inset of Fig. 9a shows the galvanostatic charge/discharge curves for the first three and last three cycles. The retained capacity of the electrode was 89% of the initial capacity after 5000 cycles at a current density of 1 A·g^{−1}, suggesting that the Faradaic reactions that occurred were reversible, with negligible ohmic drop (0.07 V) during the later cycles. Fig. 9b shows that the F2 electrode provides high energy and power densities. The energy densities of the F2 electrode were 167 and 66 Wh·kg^{−1} for power densities of 0.75 and 7.5 kW·kg^{−1}, respectively. In contrast, for the same power densi-

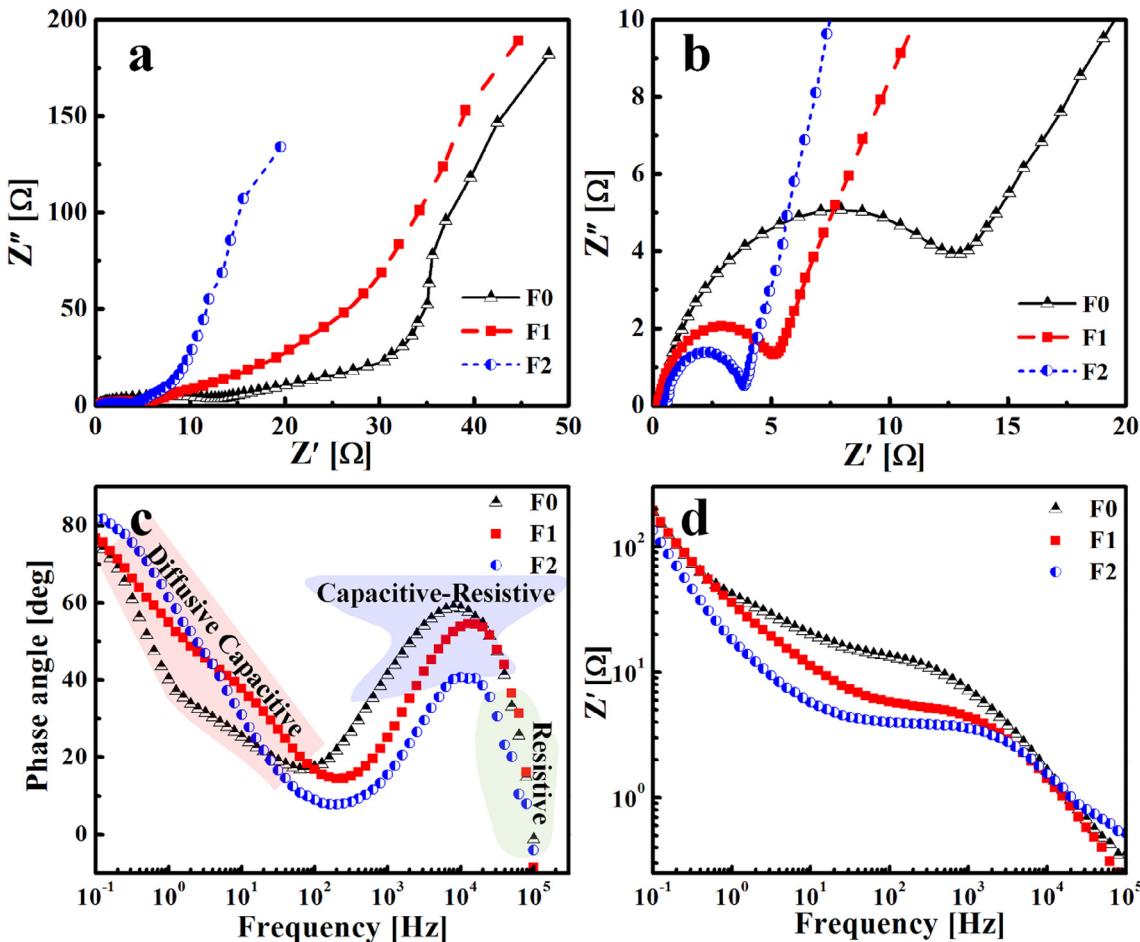


Fig. 10. Electrochemical impedance spectroscopy results: (a) Nyquist plots, (b) magnified Nyquist plots, (c) Bode phase angle, and (d) Bode impedance plots for F0, F1, and F2 at various frequencies.

ties, F0 showed energy densities of 55 and 23 Wh·kg⁻¹, respectively. The increased energy density for the same power density is attributable to the pores generated by pyrolysis of PMMA, which improved the ionic conductivity. This is supported by the fact that, for the same power density, F1 exhibited an energy density that lay between those of F0 and F2 (see Fig. 9b). However, with larger concentration of PMMA the specific capacitance significantly decreased as shown in Fig. 8d. Due to this lower specific capacitance, the energy density obtained for F3 was much lower than that of F2.

The CV curves of F2 for 5000 cycles are shown in Fig. 9c. The CV curves for $N = 1, 1500, 3000, 4000$, and 5000 indicate that the FeO_x/CNF electrode was highly stable. The circles indicate the capacitance retention, which was as high as 82%. On the other hand, the stars indicate the specific capacitance for various values of N . The capacitance decreases from 425 to 347 F·g⁻¹ at 10 mV·s⁻¹; however, the shape of the CV curves remains unchanged (inset of Fig. 9c), indicating that the reactions that occur during the cycling process are highly stable and reversible. Fig. 9d shows a light-emitting diode (LED) test performed using two symmetric FeO_x/CNF composite-based supercapacitors. The initial driving voltage for glowing LED was set to be 2.1 V. The glowing persisted for more than 50 s. The fabricated supercapacitors were highly flexible, and the LED continued to glow even when the supercapacitors were bent at an angle of approximately ~75°, as shown in Fig. S8.

Electrochemical impedance spectroscopy measurements were performed over frequencies ranging from 0.1 Hz to 100 kHz. The results are shown in the form of Nyquist plots in Fig. 10a and b (magnified view of high frequency region). The impedance response at higher frequencies is semicircular. At values of the real impedance of 3.9, 5.2 and 13 Ω for F2, F1 and F0 respectively, the Nyquist plot shows a sharp, near-vertical, increase in imaginary impedance that is characteristic of ideal capacitors. This suggests that the symmetric supercapacitors based on samples F0, F1, and F2 exhibited good capacitive behavior. However, for F0, the impedance curve ($Z' = 13\text{--}29\ \Omega$) indicates Warburg resistive behavior and subsequently transitions to the unswerving capacitive mode. The portion of the Nyquist plot (F0) with an inclination angle of 45° indicates the resistance to ion movement. On the other hand, for F2, the plot is aligned along the vertical axis, indicating that, in this sample, the ions could move more freely and that the length of the ion diffusion path was shorter, resulting in a higher specific capacitance. The shortening of ion diffusion path results in the ready transfer and accumulation of charge at the electrolyte/electrode interface.

Fig. 10c shows the phase angle responses of the various composite samples for varying frequencies. The response curve can be broken into three regions, namely, the diffusive capacitive region, the capacitive-resistive region, and the resistive region, as one moves from low to high frequencies. The longer the diffusive capacitive region, the higher is the pseudocapacitance of the electrode. On the other hand, a shorter resistive region indicates that the electrode in question is ideal for use in SCs. Further, a shorter resistive region indicates that the CNFs have contributed significantly to improving the conductivity of the FeO_x nanoparticles. Finally, Fig. 10d shows that F2 exhibits a lower modulus of impedance ($|Z|$) in the low-to-medium frequency range; this is consistent with its lower impedance and the fact that its Nyquist plot contained the smallest arc (see Fig. 10b).

4. Conclusions

Binder free, flexible, freestanding FeO_x/CNF composite mats were synthesized for use as an electrode material in supercapacitors. The porosity generated in the CNFs through the use of PMMA as a sacrificial template (porogen) resulted in the shortening of the

diffusion path for ion transport at the electrode/electrolyte surface. As a result, the composite exhibited the high retention rate of 82 and 89% at a scan rate of 10 mV·s⁻¹ and a current density of 1 A·g⁻¹ respectively, even after 5000 cycles.

Acknowledgement

This research was supported by Global Frontier Program through the Global Frontier Hybrid Interface Materials (GFHIM) of the National Research Foundation of Korea (NRF) funded by the Ministry of Science, ICT & Future Planning (2013M3A6B1078879). This research was supported by the Technology Development Program to Solve Climate Changes of the National Research Foundation (NRF) funded by the Ministry of Science, ICT & Future Planning (2016M1A2A2936760) and NRF-2017R1A2B4005639.

Appendix A. Supplementary data

Supplementary data associated with this article can be found, in the online version, at <http://dx.doi.org/10.1016/j.cej.2017.07.063>.

References

- [1] H. Choi, H. Yoon, Nanomaterials 5 (2015) 906–936.
- [2] X. Xia, Q. Hao, W. Lei, W. Wang, D. Sun, X. Wang, J. Mater. Chem. 22 (2012) 16844.
- [3] A.W.A. Ullah, A. Majeed, A. Sharif, Rehana Sharif, P. Khalid, G. Mustafa, A. Khan, Mater. Technol. Adv. Funct. Mater. 30 (2015) 144–149.
- [4] C. Fu, A. Mahadevagowda, P.S. Grant, J. Mater. Chem. A 3 (2015) 14245–14253.
- [5] H.D. Liu, J.L. Zhang, D.D. Xu, L.H. Huang, S.Z. Tan, W.J. Mai, J. Solid State Electrochem. 19 (2015) 135–144.
- [6] G. Binitha, M.S. Soumya, A.A. Madhavan, P. Praveen, A. Balakrishnan, K.R.V. Subramanian, M.V. Reddy, S.V. Nair, A.S. Nair, N. Sivakumar, J. Mater. Chem. A 1 (2013) 11698.
- [7] X.G. Xiaoping Cheng, Zhiqiang Lin, Yongjia Zheng, Ming Liu, Runze Zhan, Yuan Zhu, Zikang Tang, J. Mater. Chem. A 3 (2015) 20927.
- [8] H. Nan, L. Yu, W. Ma, B. Geng, X. Zhang, Dalton Trans. 44 (2015) 9581–9587.
- [9] Z.Y. Xia, D. Wei, E. Anitowska, V. Bellani, L. Ortolani, V. Morandi, M. Gazzano, A. Zanelli, S. Borini, V. Palermo, Carbon 84 (2015) 254–262.
- [10] N.C. Abeykoon, J.S. Bonso, J.P. Ferraris, RSC Adv. 5 (2015) 19865–19873.
- [11] J. Biscoe, B. Warren, J. Appl. Phys. 13 (1942) 364–371.
- [12] L. Liu, J. Lang, P. Zhang, B. Hu, X. Yan, ACS Appl. Mater. Interfaces 8 (2016) 9335–9344.
- [13] X. Mao, X. Yang, J. Wu, W. Tian, G.C. Rutledge, T.A. Hatton, Chem. Mater. 27 (2015) 4574–4585.
- [14] P.M. Kulal, D.P. Dubal, C.D. Lokhande, V.J. Fulari, J. Alloy Compd. 509 (2011) 2567–2571.
- [15] D.B.R. Turcu, L. Vekas, N. Aldea, D. Macovei, A. Nan, O. Pana, O. Marinica, R. Grecu, C.V.L. Pop, Roman. Rep. Phys. 58 (2006) 359–367.
- [16] K.K. Karthikeyan, P. Biji, Microporous Mesoporous Mater. 224 (2016) 372–383.
- [17] S.-Y. Wang, K.-C. Ho, S.-L. Kuo, N.-L. Wu, J. Electrochem. Soc. 153 (2006) A75.
- [18] S. Faraji, F.N. Ani, J. Power Sources 263 (2014) 338–360.
- [19] B. Sethuraman, K.K. Purushothaman, G. Muralidharan, RSC Adv. 4 (2014) 4631–4637.
- [20] T. Cottineau, M. Toupin, T. Delahaye, T. Brousse, D. Bélanger, Appl. Phys. A 82 (2006) 599–606.
- [21] K.K. Lee, S. Deng, H.M. Fan, S. Mhaisalkar, H.R. Tan, E.S. Tok, K.P. Loh, W.S. Chin, C.H. Sow, Nanoscale 4 (2012) 2958–2961.
- [22] H. Xia, Y. Shirley Meng, G. Yuan, C. Cui, L. Lu, Electrochim. Solid-State Lett. 15 (2012) A60.
- [23] M. Zhang, J. Sha, X. Miao, E. Liu, C. Shi, J. Li, C. He, Q. Li, N. Zhao, J. Alloy Compd. 696 (2017) 956–963.
- [24] X. Zheng, X. Yan, Y. Sun, Y. Yu, G. Zhang, Y. Shen, Q. Liang, Q. Liao, Y. Zhang, J. Colloid Interface Sci. 466 (2016) 291–296.
- [25] C.-H. Xu, P.-Y. Shen, Y.-F. Chiu, P.-W. Yeh, C.-C. Chen, L.-C. Chen, C.-C. Hsu, I.C. Cheng, J.-Z. Chen, J. Alloy Compd. 676 (2016) 469–473.
- [26] N. Sinan, E. Unur, Mater. Chem. Phys. 183 (2016) 571–579.
- [27] M. Aadil, W. Shaheen, M.F. Warsi, M. Shahid, M.A. Khan, Z. Ali, S. Haider, I. Shakir, J. Alloy Compd. 689 (2016) 648–654.
- [28] J. Wu, A. Zhou, Z. Huang, L. Li, H. Bai, Chin. J. Chem. 34 (2016) 67–72.
- [29] L. Wang, H. Ji, S. Wang, L. Kong, X. Jiang, G. Yang, Nanoscale 5 (2013) 3793–3799.
- [30] M. Nasibi, M.A. Golozar, G. Rashed, Mater. Chem. Phys. 139 (2013) 12–16.
- [31] Z. Wang, C. Ma, H. Wang, Z. Liu, Z. Hao, J. Alloy Compd. 552 (2013) 486–491.
- [32] A. Abdi, M. Trari, Electrochim. Acta 111 (2013) 869–875.
- [33] M. Nasibi, M.A. Golozar, G. Rashed, Mater. Lett. 85 (2012) 40–43.
- [34] M.-S. Wu, R.-H. Lee, J. Electrochim. Soc. 156 (2009) A737.